Potential for Precision Measurement of Solar Neutrino Luminosity by HERON

Y.H. Huang, R.E. Lanou, * H.J. Maris, G.M. Seidel, B. Sethumadhavan, † and W. Yao ‡

Department of Physics, Brown University, Providence, RI 02912, USA

Abstract

Results are presented for a simulation carried out to test the precision with which a detector design (HERON) based on a superfluid helium target material should be able to measure the solar pp and ^{7}Be fluxes. It is found that precisions of $\pm 1.68\%$ and $\pm 2.97\%$ for pp and ^{7}Be fluxes, respectively, should be achievable in a 5-year data sample. The physics motivation to aim for these precisions is outlined as are the detector design, the methods used in the simulation and sensitivity to solar orbit eccentricity.

1. Introduction

This paper presents an analysis of the projected capability of a detector design, HERON [1], based on a target material of superfluid helium to make a precise measurement of both the pp and ^{7}Be solar neutrino fluxes ($\Phi_{\rm pp}$ and $\Phi_{\rm Be}$, resp.) in a single, real-time experiment. The detection reaction used would be the elastic scattering of neutrinos by electrons (ES). In addition to the novel use of helium, the detector also includes the novel application of a coded aperture [2,3] technique for accurate measurement of the location and recoil energy of each elastic scattering event and to aid in background discrimination. According to models of the Sun [4], the neutrinos from the pp-I and pp-II branches of the fusion chain (known as the pp and ^{7}Be neutrinos, respectively) are, when taken together, $> 98\%$ of the neutrino flux and are associated with the reactions producing a similar fraction of the solar energy. At the present writing there have been no real-time experiments to measure the flux and spectra of $\Phi_{\rm pp}$ but recently the Borexino collaboration has made the first real-time spectral detection of $\Phi_{\rm Be}(861\,{\rm keV})$ [5]. As we explain in Sec. 2 there are several important physics issues which can be addressed if a detector can be constructed to measure both these fluxes and spectra with sufficient precision. For the pp neutrinos ($< 420\,{\rm keV}$) there does not yet exist any detector with demonstrated feasibility to measure either their flux or spectra; however, there are a number of efforts [1,6] which aim to do so.

Section 2 of this paper discusses the physics goals motivating the HERON detector. Sec. 3 briefly presents the requirements for and description of the HERON detector design. Sec. 4 and 5 provide the details of the HERON capability analysis. In an Appendix we discuss an application to measuring the solar orbit eccentricity.

2. Physics Goals

A principal goal of HERON would be to make an accurate measurement of the luminosity of the Sun using precise measurements of active neutrino fluxes. An experiment capable of measuring both $\Phi_{\rm pp}$ and $\Phi_{\rm Be}$ sufficiently well for an accurate luminosity measurement can also address several other interesting topics. These include testing for the relative rates of the ^{3}He(^{4}He, 2p)^{4}He and ^{3}He(^{4}He, γ)^{7}Be reactions which terminate the pp-I and pp-II branches in the Sun and also for testing the MSW effect (after Mikheyev, Smirnov, Wolfenstein [7]) in the LMA (large mixing angle) solution

* Corresponding author.
Email address: lanou@hep.brown.edu (R.E. Lanou).
† Now at: Intel Corporation.
‡ Now at: Magnet Laboratory, Mass. Inst. of Tech.

to the "solar neutrino problem". Additionally, if new measurements of Φ_{pp} and Φ_{Be} are successful at the few-percent level then, via new, luminosity-constrained global fits to all neutrino data, some modest improvement can be made in the knowledge of $\tan^2\theta_{12}$, $\sin^2\theta_{13}$ and limits on sterile neutrinos. Lastly, since a real-time low-energy solar neutrino experiment opens a new window in neutrino physics, the possibility of surprises in the physics should not be discounted.

2.1. *Solar Luminosity. Why measure the solar luminosity by neutrinos?*

The radiant photon energy reaching the Earth from the Sun (the irradiance, I_E) is believed to result from the nuclear fusion reactions of light elements. The energy released in each of the chains producing neutrinos is well known from laboratory experiments. Consequently, if the flux of the associated neutrinos can be determined then the photon irradiance and luminosity can be inferred from those fluxes.

This is usually formulated [8] as:

$$\frac{L_\odot}{4\pi(\mathrm{A.U.})^2} = I_E \quad \text{and} \quad \frac{L_\odot(\nu)}{4\pi(\mathrm{A.U.})^2} = \sum_i(\alpha_i\Phi_i) \qquad (1)$$

where $L_\odot$ is the total solar luminosity in photons, (A.U.) is the average Earth-Sun distance, I_E is the mean irradiance determined by Earth-orbit satellites to be $1358.8\,\mathrm{W\,m^{-2}}(8.482\times10^{11}\,\mathrm{MeV\,cm^{-2}\,s^{-1}})$ with a systematic uncertainty of about 0.4% [8,9,10]. The α_is are the coefficients giving the energy provided by and associated with the *i*-th neutrino flux Φ_i and $L_\odot(\nu)$ is the total solar luminosity inferred from the neutrino fluxes.

If the Sun operates as we presently think it does [10,11,12] then the ratio $L_\odot(\nu)/L_\odot$ should be unity. Significant departure from that expectation would signal the presence of different sources of energy within the Sun [13,14,15]. Another important point is that, from the reaction positions in the solar interior, the energy carried by the photons and by the neutrinos reaches the Earth with a huge separation in arrival times. The neutrinos arrive directly in 8 minutes while the thermal photon energy arrives from the solar plasma after approximately 40 000 years [16]. Consequently, finding a disagreement between $L_\odot$ and $L_\odot(\nu)$ would have significant implications for environmental consequences in the long term.

Because the sum of pp (91.5%) and ^{7}Be (7.4%) neutrinos are expected to be associated with $>98\%$ of the total flux, it follows that a precision measurement of Φ_{pp}, either alone or together with Φ_{Be}, will provide the major direct test of $L_\odot(\nu)/L_\odot$. Currently this comparison is only known to about 25% [17,18].

There are additional reasons to make a more precise determination of $L_\odot(\nu)/L_\odot$: the fact that the average photon irradiance is very well measured [9,19,20] has previously led to its use as a constraint in global analyses of solar neutrino experimental data. Used first as a demonstration of possible flavor oscillations of neutrinos [21] and more recently, as additional and more precise solar and reactor neutrino experimental results have become available, as a powerful constraint to aid in establishing best present knowledge of solar neutrino mass-mixing parameters and individual fluxes [17,22,23,24,25,26].

At the same time, the Standard Solar Models (SSM) [10,11,12] have continued to make significant improvements so that quite precise predictions for the fluxes have been made. For example, Φ_{pp} is predicted to $\pm1\%$ and Φ_{Be} to $\pm9.5\%$ [11] [1]. When these predictions are compared against the fluxes found from global fits to all of the existing solar and reactor data [28] the levels of agreement differ significantly depending on whether the photon luminosity is used as a constraint or not. For example, the ratios of global-fit fluxes to SSM predictions are (at 1σ): for pp, 1.01 ± 0.02 and for ^{7}Be $1.03^{+0.24}_{-1.03}$ *with the luminosity constraint* but are $1.38^{+0.18}_{-0.25}$ and $0.13^{+0.41}_{-0.13}$, respectively, *without the constraint* and leads to the poor knowledge of $L_\odot(\nu)/L_\odot$ noted above [17,24,25,26,29].

The question of how precisely direct measurements, of either Φ_{pp} or Φ_{Be} must be made in future experiments has been cogently addressed in an important paper by Bahcall and Peña-Garay [17]. Related and more recent considerations also have been made by others [11,18]. The level of precision required depends strongly upon the specific physics questions to be addressed. In all cases, the demands on experimental techniques are severe. For example, the authors of Ref. [17] carried out simulations of global analyses utilizing all present data plus inclusion of potential future pp and ^{7}Be experiments with assumed capability of precisions ranging from 1% to 30% (at 1σ). They find that a ^{7}Be result of $\pm5\%$ could improve knowledge of $L_\odot(\nu)/L_\odot$ from $1.4^{+0.2}_{-0.3}$ to 1.07 ± 0.13. Increased precision on ^{7}Be alone would not yield further improvement; while a $\pm1\%$ on pp could achieve a remarkable 0.99 ± 0.02 on the lumi-

[1] Note 1: 8.5% of the 9.5% is contributed from the experimental uncertainty in S_{34} nuclear cross-section factor; however, new data from the LUNA collaboration [27] suggests this contribution may be reduced to 2.5%. Private communication C. Peña-Garay.

nosity comparison by neutrinos. The authors note that a result of this accuracy would be *"a truly fundamental contribution to our knowledge of stellar energy generation and place a* $\pm 2\%$ *bound on all sources of energy other than low energy fusion of light elements (i.e., pp and CNO chains)"*. The HERON detector, as shown in the present paper, is intended to be capable of reaching precisions on both fluxes commensurate with these goals.

2.2. *The pp-I vs pp-II and LMA-MSW*

The relative magnitude of Φ_{pp} versus Φ_{Be} is a particularly relevant parameter, on the one hand, bearing on the accuracy of the SSM and, on the other, as evidence for the MSW effect in the LMA. It is valuable to have an experiment which measures both Φ_{pp} and Φ_{Be} since several systematic errors tend to cancel in the ratio Φ_{Be}/Φ_{pp}. In the SSM there is a very strong anti-correlation between the two fluxes with a coefficient of -0.79 to -0.81 [11]. If the $^3\mathrm{He}(^4\mathrm{He},\gamma)^7\mathrm{Be}$ reaction of the pp-II chain were the only terminating branch, only one pp and one ^{7}Be neutrino would be produced in each cycle. Otherwise there would be two pp and no ^{7}Be neutrinos if $^3\mathrm{He}(^3\mathrm{He},2\mathrm{p})^4\mathrm{He}$ of the pp-I branch were the terminating reaction of the full fusion cycle. What the actual relative reaction rates are depends on several not yet accurately known details within the Sun such as elemental abundances, temperatures and density. (Present versions of the SSM predict a ratio of the two reaction rates as 0.174 [24] which implies, prior to oscillation, a value of 0.080 for Φ_{Be}/Φ_{pp}.) An independent and precise measurement of these relative rates would be an important contribution to the understanding of stellar processes and would permit a refinement of the use of the SSM in global analyses of neutrino data. The physics of the MSW effect [7] is embodied in the flavor-dependent interaction differences for neutrinos propagating in matter as opposed to vacuum. Due to the differences in neutrino energies and solar density at their production points the pp, ^{7}Be and ^{8}B neutrinos are expected to have quite different survival probabilities. The LMA-MSW solution specifies what this energy dependence must be.

The oscillations of the much higher energy ^{8}B neutrino should be strongly suppressed by matter dominance and the pp neutrinos much less since they should be vacuum-dominated. The ^{7}Be and pep neutrinos, having energy intermediate to pp and ^{8}B, are in the crucial energy region where the transition between matter dominance and vacuum oscillations is to be expected. The ^{8}B flux is now very well measured by the Super Kamiokande (SK) and Sudbury (SNO) experiments [in Ref. [28], see e.g. Fukuda et al. and Ahmed et al.]; however, direct experimental evidence for this MSW transition is still lacking and could be provided by an experiment such as HERON.

2.3. *Other areas of interest related to neutrino properties*

The Φ_{pp} and Φ_{Be} measured in ES are, by necessity, the fluxes of active neutrinos. Consequently, in the measurement of $L_\odot(\nu)/L_\odot$ an alternative interpretation of a result consistent, within errors, to unity can be taken as the establishment of a limit on the presence of sterile neutrinos.

Due largely to the lack of precision experiments on these two major low-energy fluxes, there has been some leeway in the recent analyses of the solar and reactor data which allows for consideration of several well-motivated proposals for "new physics" in the neutrino sector. Among these are possibilities for non-standard neutrino interactions with their environments (NSI) [30]. Within this class of models the additional effects to be expected are strongly constrained by existing data; however, in some cases they should be most pronounced in the energy dependence of the fluxes of solar neutrinos $< 1\,\mathrm{MeV}$. In these cases the effect is qualitatively similar, but differs quantitatively, from that to be expected from the LMA-MSW transition in the matter- to vacuum-dominated neutrino energy regions. Two examples of this class, are models with flavor-non-conserving neutral currents [31] or with mass-varying-neutrinos ("MaVaNs") [32]; the latter inspired by possible insights into understanding "dark energy". Confirmed evidence found for NSI would place our knowledge for the mass-mixing parameters in doubt; alternatively, such precision measurements of the matter-vacuum transition region would also serve to establish new limits on the existence of NSI.

New measurements of low energy solar fluxes can play only a rather limited role in improving on present knowledge of $\tan^2\theta_{12}$ and $\sin^2\theta_{13}$ limits. To be useful, the new data would need to be folded into a comprehensive analysis with all the other data (solar, atmospheric and reactor) which from present data have already established impressive errors on the parameters [18,23,26,33]. The potential for improvement in these parameters by low energy ES or CC experiments has been subjected to a detailed study by the authors of Ref. [17] who conclude that without new physics even

$\pm 1\%$ on Φ_{Be} would make a negligible improvement on $\tan^2\theta_{12}$ and a Φ_{pp} result $< \pm 3\%$ is required to improve the error by more than 15%. The authors' conclusions on any improvements to be expected on $\sin^2\theta_{13}$ are similar.

3. Detector

3.1. *Requirements*

There are stringent requirements placed on any detector designed to achieve these goals. In order to be sensitive to all active neutrino flavors, the detection reaction is that of the elastic scattering from atomic electrons (ES) in the target: $\nu_{e,\mu,\tau} + e^- \rightarrow \nu_{e,\mu,\tau} + e^-$. The ES event signature is the occurrence of only a single, low energy recoiling electron in the detector medium. The recoil spectra are continuous from zero with the pp decreasing monotonically to a maximum energy of 261 keV while the ^{7}Be spectrum is nearly flat up to 664 keV maximum (see points labeled input in Fig. 4). These recoil spectra place a premium on achieving as low an energy threshold as possible. The most dangerous backgrounds are those which can be created by the appearance of electrons from Compton recoils of gamma rays or radioactive decays within the medium of the target. These backgrounds need to be mitigated by a combination of event signatures, use of low activity materials, depth and shielding. In order to achieve the desired few-percent precision, very large statistics event samples are required and systematic errors arising from effects due to analysis cuts (e.g., fiducial volume, thresholds, pp and ^{7}Be event separation, calibrations) must be minimized. Although these details emphasize the challenges to be faced in constructing an operating detector, there are two mitigating factors: the ES cross-section is very precisely known due to experiment and electro-weak theory and the expected fluxes are high ($\Phi_{pp} = 5.99 \times 10^{10}$ and $\Phi_{Be} = 4.84 \times 10^9\,\mathrm{cm^{-2}s^{-1}}$ [11]). Typically, this will result in an ES event rate of $\sim$ 2 events $\cdot$ tonne-day^{-1} which implies that only a modest-size fiducial volume (e.g., $\sim$ 10 tonne) is needed for a high statistics experiment.

3.2. *HERON configuration and detection processes.*

The detector design is shown in (Fig. 1) and its design is discussed in more detail in Ref. [1,34,35] . The general approach of HERON to these issues is as follows. The target material chosen is ^{4}He in the superfluid state (density 0.145 g/cc) which has several beneficial

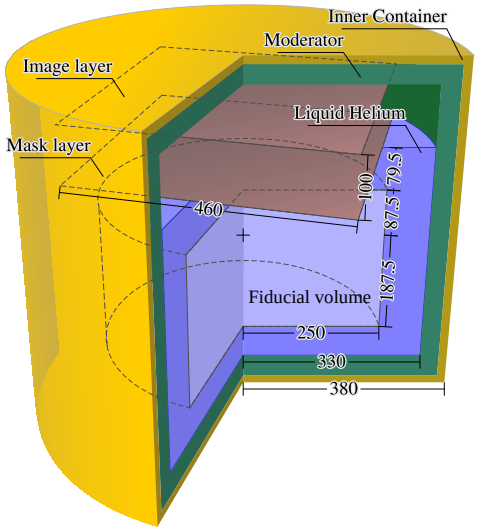

Fig. 1. The geometry of the HERON detector design, all dimensions are in centimeters.

properties. Energy deposited in the helium by recoiling particles can be detected by one or all of three processes: scintillation, phonons/rotons or collecting the recoil electron trapped in a bubble. Helium has no long-lived isotopes but more importantly it can be made absolutely free of all other atomic species. At superfluid temperatures it is self-cleaning of impurities due to their high mobility and favorable energy minimum at the container walls. Even particulate matter quickly attaches to the container walls at our operating temperature of $\sim$ 30–50 mK. Since the bulk helium volume will be free of background sources, the concern is to counter radiation entering from the cryostat (27.3 tonne copper) and its environment. In a separate study environmental sources were modeled with the detector cryostat actively shielded externally by 3.5 m of water at a rock overburden of 4500 meter-water-equiv. (m.w.e.). Helium is virtually immune to creation of long-lived cosmogenic muon activity, capture or decay in it; muons ($4\,\mathrm{m^{-2}day^{-1}}$ at 4500 m.w.e.) are vetoed externally and internally in any case and greater depth is possible. This was sufficient shielding against environmental neutrons, cosmic muons and gammas that, for purposes of the analysis simulation under consideration here, they would be negligible relative to sources from the cryostat and other detector parts. As a consequence the background issue reduces to controlling conversions of gammas entering the helium volume of 21.6 and 8 tonnes total and fiducial, respectively. However, helium does not have good self-shielding properties and this is partially compensated for by lining the cryostat with a moderator of solid nitrogen enclosed in acrylic cells (5.6 T acrylic

and 104 T solid nitrogen, density 1.03 g/cc). The function of the moderator is to absorb or degrade in energy by Compton scattering the entering gamma rays which originate 97% and 3% from the cryostat and moderator, respectively. The flux of gammas entering the helium is dominated by low energy (dominantly < 1 MeV) cosmogenic activity in the copper with the remainder from U, Th and other activity in the copper, nitrogen, acrylic and other parts. The background gamma conversions in the helium cannot be fully eliminated but are amenable to the development of a distinguishing signature which aids in their separation from signal; the nature of this separation is detailed in Sec. 4 and 5.

We have chosen to use as the basic elements of detection for both signal and background the collection of scintillation light and also the recoil electron trapped in its bubble. We have carried out studies of these processes using prototype calorimeter sensors/detectors developed for this project and suitable for both signal types; the processes and results are discussed briefly below and in more detail in the references cited.

Excited or ionized He atoms along the electron path quickly form dimers in the liquid. The radiative decays to the ground states of these singlet and triplet dimers emit photons in the ultraviolet. The scintillation light is in a narrow band centered at 16 eV and results from the decay of the singlet dimer $He_2^*(A^1\Sigma_u^+)$ [36]; since this energy is lower than the first excited state of He at 20.6 eV, the liquid is self-transparent. 35% of a recoil electron's energy is released (~ 27000 photons/MeV) in this singlet dimer mechanism [34]; the energy from the long-lived (~ 15 sec) triplet dimer escapes or is collision quenched. (An additional 43% of the recoil energy is radiated in phonons and rotons which by quantum evaporation [37] could in principle also be utilized with the calorimetric sensors for discrimination [38]; however, we find incorporating into event signatures the detection of the recoil electron from the drifted bubble a much stronger discriminant.)

When a recoil electron in He has lost most of its energy it forms an electron bubble. The electron experiences a strong, short-range repulsive potential from the bound electrons on surrounding atoms due to Pauli exclusion. This repulsion forms a vacant volume, or bubble, of 19 Å radius in which the electron is confined. The bubble forms in about 10 pico-sec with an effective displacement mass of ~ 500 He-masses and has a hydrodynamic mass of half that [39]; consequently due to this difference in masses, under gravity and with no electric field, a bubble would experience a buoyant acceleration of $\sim 2g$. A uniform drift velocity of the bubble can be provided and controlled by a combination of applied electric field and a very low concentration of ^{3}He; for example, at 40 mK, 30 ppm ^{3}He and a field of 300 V/m provides a drift velocity of 17.5 m/s. In a worst case example of 5 m (maximum depth), the 3×10^8 collisions induced due to the large cross-section of ^{3}He for scattering a bubble leads to an uncertainty in the transit time of 16 μs and hence to a depth error of < 1 mm. In addition to providing a "drag" force the ^{3}He also aids in extracting the electron efficiently through the free surface of the liquid by vortex attachment (Surko and Reif [40]). Two grids on either side of the liquid surface (not shown in Fig. 1) provide the drift and extraction fields [43]. (At the normal operating temperature of 30–50 mK the vapor pressure is sufficiently low that the space above the liquid is effectively a vacuum.) The final grid accelerates the electron to ~ 1 keV thus providing a large and distinguishable pulse in the calorimeter.

For several reasons, photo-multiplier tubes (PMT) are not suitable event detectors for HERON, among them: the high radioactivity of PMT's, poor He self-shielding, lack of transparency of moderator and the desire to detect the drifted electrons. As mentioned, both scintillation and drifted electrons are detected on the same calorimetric devices. Each device constitutes a pixel in a geometric array (a coded aperture) and consists of a thin wafer of silicon or sapphire to which is attached a high sensitivity metallic magnetic calorimeter (MMC) read out with a SQUID sensor [41]. For astrophysical x-ray application, versions of MMC have been constructed with ~ 3 eV resolution [42]. Projecting from measurements on wafer prototypes of smaller heat capacity to ones of the HERON size, ~ 10 eV resolution is to be expected. In a full simulation of the response of this large wafer ($100 \times 100 \times 0.4$ mm, in this example) with 16 eV photons it is found that single photons should be detectable at wafer temperature of 40 mK producing a pulse of 5 ms rise- and 100 ms fall-time [44]. This performance capability is assumed in the context of the analysis of Sec. 4 and 5.

For each neutrino event we must reconstruct its position within the He and also its recoil electron energy. In addition, we must develop event signatures which aid in separating signal from background events. The maximum track length expected for a neutrino event is ~ 2 cm so that on the scale of the total helium volume (149 m^3; 21.6 T) neutrino signal events are effectively point sources of scintillation light. At the dominantly low energies of the gamma-ray background events the conversions in He are overwhelmingly (95%) Compton scatters. 90% of these conversions are multiple depositions distributed over an average length of more than 50 cm in the He. Consequently, the scintillation

from background arises from a distributed, rather than a point, source; additionally the event most often contains multiple, un-recombined electron recoil bubbles. These latter two features constitute the primary background signature. Subsequently, differences among the spectral and spatial distributions of the signal and residual background events facilitate their final separation. In order to create these signatures and to enable the necessary cuts on data samples the 2400 wafer calorimeters are arranged into two planes in the vacuum space above the liquid; the resulting array constitutes a coded aperture and provides the ability for both spatial and energy reconstruction.

4. Nature and use of HERON's coded aperture.

4.1. *General principles.*

The concept of coded aperture arrays [2,3] has been a well established one with arrays being widely used in x-ray astronomy . The role of the array is to accurately determine the *direction* of incoming photons from a remote x-ray point source. A coded aperture array consists of two parts, an imaging plane and, separated by a fixed distance, a mask plane. In the x-ray application the image plane consists of a set of active sensors (or pixels) while the mask plane is opaque with a pattern of cut-out apertures. For far-distant sources, nearly parallel rays enter the array and some of them are blocked by the opaque portions of the mask; thus the image imposed on the sensor plane will resemble the pattern of the apertures in the mask effectively leaving a "shadow" (See Fig. 2). In principle, to determine the direction of the light source it is simply a matter of comparing the shadow pattern to that of the mask itself. In practice, elegant techniques have been developed for design of mask patterns and image deconvolution taking into account side-lobe effects as well as intrinsic and statistical noise. Various classes of mask patterns have been employed in the x-ray field ranging from random apertures to strictly repeating and regular patterns. The choice of one over another depends upon experimental considerations such as strength of photon flux, resolution needed and sidelobe tolerance.

In the HERON application there are important differences: a) a non-distant point source location is to be determined within a limited volume in *3-D*, b) the event energy must be measured, c) for reasons (a) and (b) both planes will consist of active wafer pixels and d) some discrimination is needed between point and non-point sources. The HERON coded aperture array is arranged

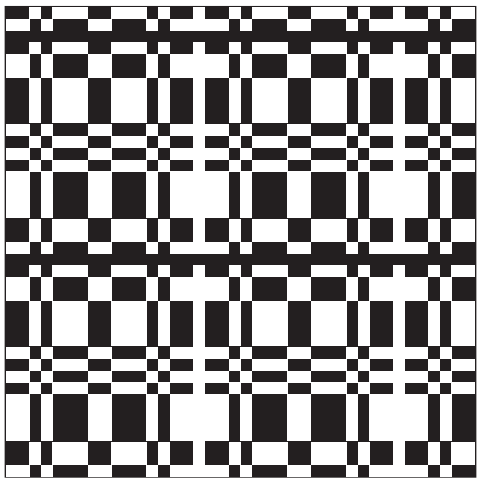

Fig. 2. URA pattern, 40×40 in dimensions and 19×17 in periodicity. Dark and light areas represent opaque and open regions, resp. In the HERON mask, the smallest squares represents single wafers.

with the mask plane 1 cm above the liquid surface and the image plane 1 m above the mask. The pixels are arranged in 40×40 square arrays (460×460 cm each) with 1600 wafer calorimeters in the image plane and 800 in the mask. The pattern of apertures in the mask is that of a uniformly redundant array (URA) [3]. This mask pattern was chosen because of its low intrinsic noise and high transparency (50%). (In the notation of the URA it has a (17,19) grid spacing [3] as shown in Fig. 2.) The nature of the URA and HERON physical properties and goals constrain the choice of wafer pixel size. The He fiducial volume can be chosen and varied during physics analysis but the total mass of He is contained within a cylindrical volume of $R = 330$ cm and 435 cm height. In our application, the transverse dimensions of the array should be at least commensurate with those of the fiducial volume containing the sources and, although smaller pixel sizes imply finer spatial resolution, ultimately photon statistics dominate (typically a few hundred photons for many neutrino events, due to energy and solid angle effects). For the HERON geometry a choice of 11.5×11.5 cm pixels in a URA gives resolution adequate to the physics goals without unnecessarily increasing the complexity or noise and consistent with the desired single photon performance for a wafer of this size.

4.2. *Loglikelihood method for event reconstruction.*

The deconvolution techniques used for typical x-ray applications are not applicable for our 3-D application; additionally, they are not easily amenable to developing

a background (distributed source) signature. Instead we have adopted a likelihood approach along with a search algorithm for the most probable position in 3-D space.

This approach treats each event in a sample containing both signal and background as if it were a single point source. With that assumption, it finds from the observed photon hit pattern the most probable values of its spatial location and total energy. Although no attempt is made on an event-by-event basis to distinguish signal from background, distributions of the likelihood parameter's logarithm can be useful in separating signal and background as we show in Sec. 5. Similarly, the effective point-like positions and effective energy distributions of the background events are used.

Operationally, the algorithm initiates with a test-point location in the volume and the probability of this test electron to produce the observed photon hit pattern is calculated. The test photon distribution is taken as isotropic with straight-line propagation; the probability of hitting the *i*-th wafer is then proportional to the solid angle (ω_i) subtended by the wafer from the photon current starting point. After a systematic search of points throughout the available volume, the location in space found to have the highest probability is taken as the final position.

If Ω is the solid angle subtended by all m wafers in both planes and N is the number of photon hits in the pattern then we can define a quantity $N_{\rm tot} = 4\pi N/\Omega$ which is the total number inferred for the test point. Then the probability of an event located at $\mathbf{x}$ producing the recorded photon pattern is evaluated as:

$$P(\mathbf{x}) = \left(\frac{1}{4\pi}\right)^{N_{\rm tot}} \prod_{i=0}^{m} \frac{\omega_i(\mathbf{x})^{n_i}}{n_i!} \qquad (2)$$

where n_i is the number hitting *i*-th wafer and $n_0 \equiv N_{\rm tot} - N$ and for computational convenience we use the logarithm (loglikelihood):

$$\mathcal{L}(\mathbf{x}) \equiv \ln P(\mathbf{x}) = -N_{\rm tot} \ln 4\pi + \sum_{i=0}^{m} \ln \frac{\omega_i(\mathbf{x})^{n_i}}{n_i!} \qquad (3)$$

and select as the final position the one with the largest (least negative) $\mathcal{L}$. The final energy estimate is scaled from the solid angle subtended from the test point. The process converges rapidly guided by a set of empirically established criteria for avoiding subsidiary maxima and reaching a stable solution. [2]

[2] One might expect the determination of the effective solid angle and efficiency to depend on the optical properties of the UV radiation for He and the wafers. Effects resulting from: the width of the singlet dimer spectrum, internal reflection and refraction at the He surface, Rayleigh scattering, multiple reflections between He and wafers or among wafers themselves can affect the value of the effective solid angle. However, these effects are small due to the low refractive index of He (1.045), the self-transparency and very long Rayleigh mean-free-path (200 m [45]), the narrowness of the UV spectrum and the low reflectivity of the wafers at the incident angles involved [46]. These effects can be taken into account by including ray-tracing techniques and we have tested them in our analysis [35]; however, it is more computationally demanding and results in no essential differences on flux as we demonstrate in our final error table (Table 5). Consequently, for simplicity of analysis and discussion we ignore these effects in this paper.

	Cryostat	Acrylic	Solid N_2
^{238}U, ^{232}Th	2×10^{-13} g/g	4×10^{-13} g/g	$<10^{-16}$ g/g
Cosmogenics	50 μBq	—	—
^{7}Be, ^{39}Ar, ^{85}Kr	—	—	16 Bq/tonne
$K_{\rm nat}$	5×10^{-10} g/g	4×10^{-9} g/g	—

Table 1
Assumed levels of residual activity in major detector components.

4.3. *Event simulation and reconstruction*

A test of the reconstruction ability of the coded aperture approach has been done in a way which examines a full range of variable correlations. We have generated samples of pp, ^{7}Be (5×10^{5}, each) and background events (2.5×10^{6}) as they would appear in the configuration of HERON described. For the neutrinos, the input recoil electron energy spectra are as shown in Fig. 4 and the events are distributed uniformly throughout the full He volume. The input background sample in the He is generated by propagating gamma rays initiating from sources within the detector's principal components using GEANT3 [47]. The source activities and concentrations are listed in Table 1. Within the He account was taken for bremstrahlung, very low energy Compton recoils and delta-rays. For all input samples, the original position and deposited energy for every recoil electron was retained for use in comparing to reconstructed values. The events were then reconstructed as described in Sec. 4.2.

Signal reconstruction. The principal interest in this section concerns the reconstruction results for the true point sources—the pp and ^{7}Be events.

Some examples of spatial and energy resolutions (1-σ) for the reconstructed pp and ^{7}Be samples are shown in Fig. 4, 5, and 6. R_{xy} (calculated from the fitted x and y coordinates) is the horizontal position in the He cylindrical volume and E is the total deposited energy. The z-coordinate (depth) is a factor $\sim 2\times$ poorer when reconstructed by coded aperture; however, since the bubble drift time gives better than 1 mm resolution the depth

position by timing is used instead. While the results of the reconstruction are quite satisfactory, several points should be noted about the figures and the nature of the results. The resolution dependence on photon statistics is common to both energy and position and is dominant at the lowest energies, but it can also arise at higher energies as a contribution due to diminished photon solid angle from the extremities of the detector and mask geometry. As the two inserts for Fig. 5 and 6 show, the maximum value of the distributions indicate excellent agreement between input and output values, the shapes near the maxima are symmetric and the FWHM look reasonable. However, such figures are too limited to adequately illustrate the effects of correlations nor of any asymmetries in the tails. The correlations between spatial and energy variables are of major concern as they enter into flux accuracy when making the high level analysis cuts for fiducial volume and threshold. For our main purpose, the precise neutrino flux determination, it is most direct and useful to examine comparisons of the complete set of distributions to be used during the flux separation of the three channels of events. This is the case because if our model of the detector is correct the full generation and reconstruction of these samples naturally includes all of the effects of the correlations and tails and permits estimation of their contributing errors. Sec. 5 examines the question of cuts to reduce background and to make flux separations.

Background reconstruction. Any event trigger is accepted with a scintillation pulse above hardware threshold. An important point in the subsequent treatment of the events is dependent upon the detection of the electron(s). The difference in electron bubble topology (multiplicity) between background and signal is an additional key factor in reducing the raw background rate for analysis.

The nature and magnitude of the sources used in our simulation were listed in Table 1. Any event giving one or more gamma conversions anywhere in the entire helium volume is recorded and reconstructed by the coded aperture method of Sec. 4. The simulation result implies a total daily rate in the full He volume of nearly 4×10^3 events; a factor ~ 70 greater than signal. Several properties of the background depositions are useful to establish prior to making high level cuts on the samples for flux separation. These properties (multiplicity, event loglikelihood, energy and spatial distributions) were determined from the sample of 2.5×10^6 simulated events.

Due to the large size of the He volume and the low energies of the gammas entering through the moderator, the detector is essentially hermetic and in most cases fully contains the event. Because of the He density and

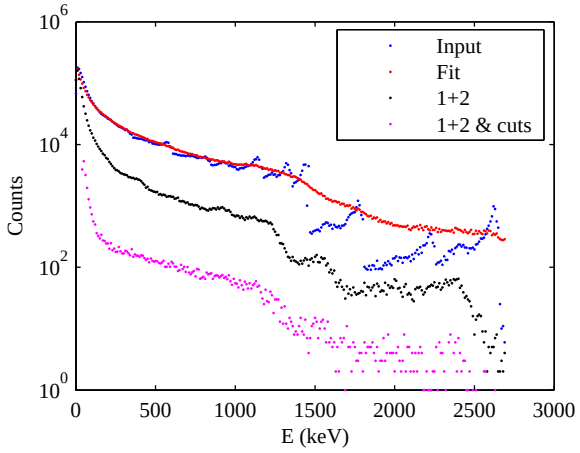

Fig. 3. Energy spectra of simulated background events. "Input" contains all events before reconstruction; "Fit" are the reconstructed energy of these events; "1+2" are the events with no more than 2 drifted electrons; "1+2 & cuts" are the "1+2" with "std" fiducial and 45 keV energy threshold cuts.

gamma mean free path a typical event, prior to cuts, consists of widely distributed Compton recoils with a mean multiplicity of 12.9 electrons and a mean spatial separation of 57.6 cm. The uncut energy deposition spectrum both before and after reconstruction is shown in Fig. 3. It should be emphasized that it is not important in our method to extract the true energy of each background event, which in any case cannot be done with a coded aperture for events of these topologies since there is no true point-origin of scintillation. In addition to providing a non-pointlike $\mathcal{L}$-value, an effective energy is obtained and this accounts for the smoothing seen in the reconstruction of the raw input spectrum for gamma conversions in Fig. 3.

In order to use the number of detected drifted electrons effectively there must be a high efficiency for collecting each one. Full 100% efficiency is not possible due to ion re-combination. As noted, for drift control purposes we envision a uniform field of modest strength (300 V/m). With this field and in our geometry very high efficiency ($\sim 85\%$) can be expected for any electron with > 5 keV [43].

As a first step in reducing the background sample for further analysis we impose an event selection criteria of multiplicity < 3 detected electrons; each with an energy > 5 keV. This reduces the background by a factor 0.38 without affecting the neutrino signal (possible bremstrahlungs from neutrino events remain included by this cut). See Fig. 3 for the resulting effect of this multiplicity cut on the spectrum. Since the goal is to extract pp and Be fluxes separately, we choose not to make an event-by-event division of neutrino events from back-

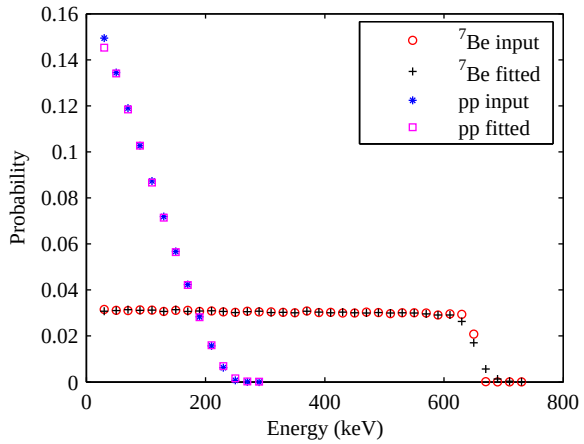

Fig. 4. Comparison between input neutrino spectra and their reconstructed counterparts. Each spectrum contains $\sim 5 \times 10^5$ simulated events and is normalized.

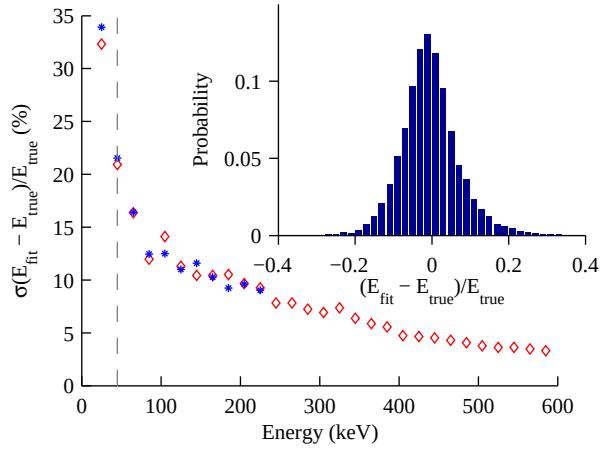

Fig. 5. Resolution of reconstructed energy for neutrino events with respect to the energy of input events (asterisks: pp; diamonds: Be). The inset shows the distribution of reconstructed energy of events between 100 and 120 keV.

ground with the likelihood ratio. Instead we defer to making the simultaneous separation of all three channels by the method described in Sec. 5. Additional samples of 8×10^5 background events with detected multiplicity < 3 are also generated. These, together with the neutrino samples, are then binned to form PDF's and used for further study of high level cuts.

5. Flux separation

Fundamental to the method of flux separation used here is the construction of accurate probability distribution functions (PDF). They present the expected appearance for four major reconstructed variables (R^2, z, energy and $\mathcal{L}(\mathbf{x})$) for events from the two neutrino signal channels and the backgrounds. The PDF's are used in an extended-maximum-likelihood method [48] applied to a simulated experimental random sample including events from all three channels. The PDF variables used are the radial and vertical positions of the events, their energies and the $\mathcal{L}$ of Eqn. 3. Our principal goal here is to examine the type of systematic errors introduced by this approach.

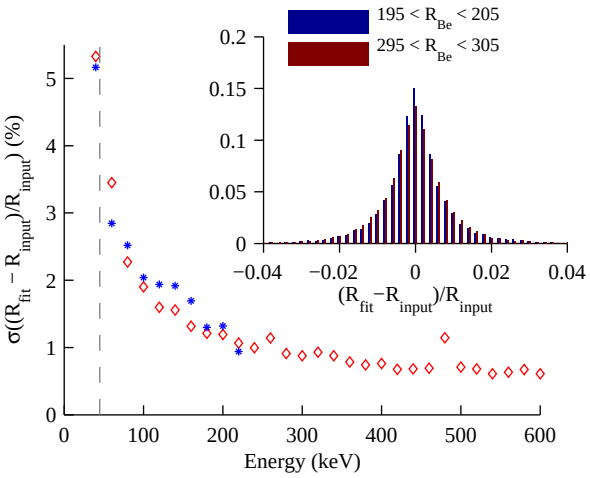

Fig. 6. Resolution of reconstructed radial position for the neutrino events depending on their energies (asterisks: pp; diamonds: Be) . The inset figure shows the distribution of reconstructed radii of events at different horizontal distances from the center of the detector.

5.1. *Fitting fluxes using likelihood method*

After we have observed and reconstructed neutrino and background events with sufficient statistics, we may separate the three fluxes (pp, ^{7}Be and background) using the extended likelihood method. Given certain binning, the extended (log)likelihood function is defined for each individual variable as

$$\mathcal{L}_\Phi = -\sum_{\alpha=1}^{3} N_\alpha + \sum_{\text{bin } i} n_i \ln \sum_{\alpha=1}^{3} N_\alpha p_{\alpha i} \qquad (4)$$

where α denotes the flux type, $p_{\alpha i}$ the probability of flux α populating the bin i, n_i the total number of events in bin i, and N_α the number of events being of type α. N_α are the parameters that are to be adjusted to maximize $\mathcal{L}_\Phi$, with the constraint that their sum equals to the observed total number of events.

The derivation and structure of error ε_α for each fitted flux N_α by this method is discussed in ([35] Appendix A). The error matrix V, defined as $V_{\alpha\beta} \equiv \langle \varepsilon_\alpha \varepsilon_\beta \rangle$, in this context evaluates to

$$V = -\mathbf{N} + \mathbf{P}^{-1}, \tag{5}$$

where elements of matrices **N** and **P** are

$$\mathbf{N}_{\alpha\beta} \equiv \delta_{\alpha\beta} N_\alpha \quad \text{and} \quad \mathbf{P}_{\alpha\beta} \equiv \sum_{\text{bin } i} \frac{p_{\alpha i} p_{\beta i}}{n_i}, \tag{6}$$

where $\delta_{\alpha\beta}$ is the Kronecker delta, with indices α and β referring to flux types.

Note that the elements in matrix **P** may have very large values if some bins have very low counts (i.e. n_i being small), which will lead to reduced numerical stability of $\mathbf{P}^{-1}$ and consequently of V. To avoid this, we chose to use a variable-width binning where bin edges are chosen so that each bin contains roughly the same number of events.

Matrix **P** describes how much one PDF resembles another. If for two fluxes α and β, $p_{\alpha i}$ and $p_{\beta i}$ are strongly correlated over index i, **P** will have large non-diagonal elements, resulting in large valued elements in $\mathbf{P}^{-1}$ and V. In other words, if two PDFs are similar in shape, the expected errors of their fitted fluxes will be high. This property dictates the variables we can use for flux separation: reconstructed R and z distributions are basically identical for both types of neutrinos, thus they are not suitable for separating ^{7}Be from pp; while energy and loglikelihood of reconstructed events provide satisfactory PDFs for this purpose.

5.2. *The PDF distributions.*

In generating the PDF's, the input pp and ^{7}Be neutrino oscillated fluxes to be expected at Earth are based on the Bahcall-Pinsonneault solar fluxes [11,12], the mass and mixing parameters from the global fit of Fogli et al [23] and assumed two-flavor mixing. 5×10^5 recoil electron events were generated for each of pp and ^{7}Be and each contained the appropriate mix of active neutrino flavors (ν_e, $\nu_{\mu\tau}$). (The resulting daily event rate above 45 keV is 1.7 pp and 0.6 ^{7}Be per tonne.) The points labeled "input" in Fig. 4 show the spectra in HERON to be reconstructed. For background 2×10^8 gamma rays due to the sources listed in Table 1 were generated and propagated via GEANT through the detector. Of these, a sub-sample of 8×10^5 with less than three conversion electrons in the He each with energies greater than 5 keV were used in creating the background PDFs. This sub-sample choice resulted from the detailed study of the properties of a full sample of conversions as outlined in Section 4.3. Shown in Figures 7–10 are samples of the four PDF's prior to any fiducial or threshold cuts.

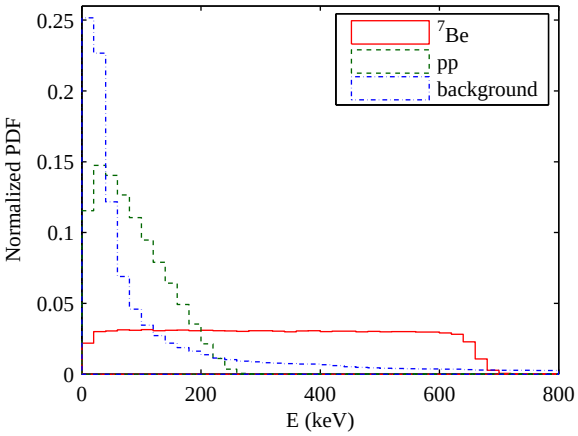

Fig. 7. Normalized PDF for reconstructed energy spectra of simulated events *before high level cuts*. These include 8×10^5 background events, and $>5\times10^5$ events in each neutrino flux.

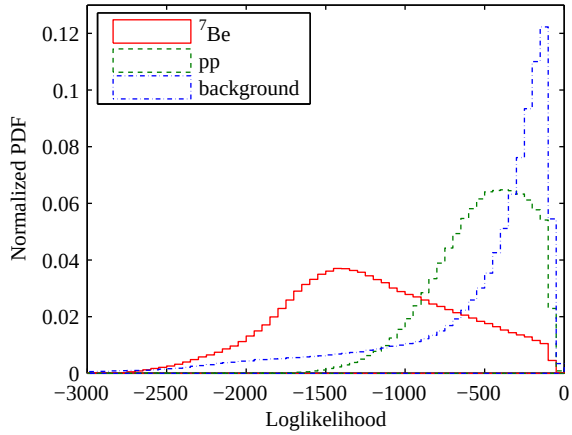

Fig. 8. Normalized PDF distribution of fitted loglikelihood of simulated events *before high level cuts*.

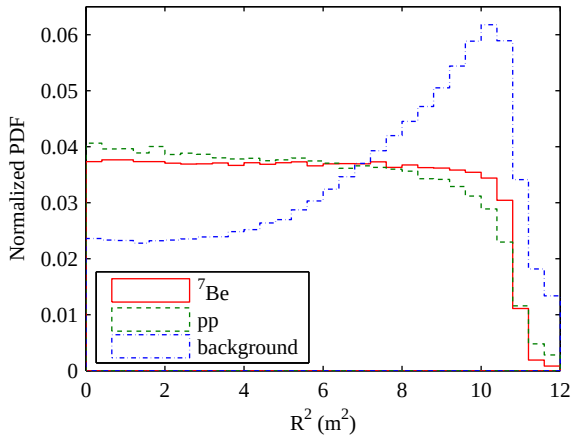

Fig. 9. Normalized PDF distribution of horizontal radii $R=\sqrt{x^2+y^2}$ for the simulated events *before high level cuts*.

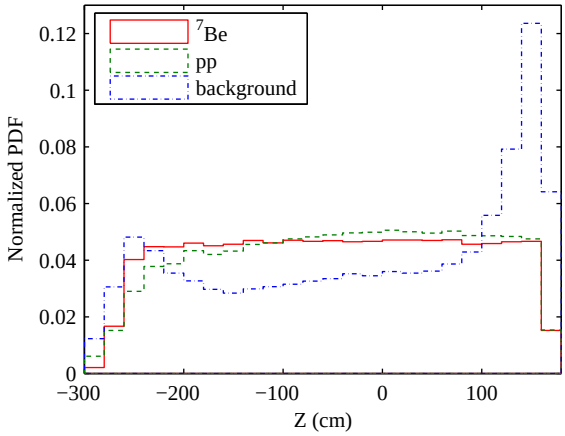

Fig. 10. Normalized PDF distribution of depth of simulated events *before high level cuts*. See Fig. 1 for the coordinate system.

5.3. *High-level cuts.*

Even after reducing background rate by rejecting events with three or more recoil electrons, the background conversion rate in the full helium volume would still be a factor ~ 25 higher than that of the neutrino recoils in the full helium volume, this factor can be significantly improved by instituting fiducial volume and energy threshold cuts.

The following considerations were made for choosing to impose these high level cuts on fiducial volume and threshold with a minimum of bias. Depending on the fraction of detector surface area covered by the coded aperture, the resolution worsens somewhat at the extreme edges. In practice the position and energy resolution will have to be carefully calibrated by temporary insertion of sources at measured locations; however, cutting in the simulation avoids possible artificially introduced features in the PDF's due to inaccuracies in the reconstruction model. Additionally, it is convenient to work with a better signal to noise ratio provided that the distinguishing characteristics among the PDF's are not compromising the sensitivity. A check on this can be seen in Table 2 and 3 where the results are presented for analyses with three quite different fiducial volumes and two differing thresholds. The contribution to flux error is not significantly changed amongst them. Our goal has been to seek an optimal set of cutting parameters that yield the lowest relative systematic uncertainty in the fitted neutrino fluxes.

The various components of errors due to the flux separation process and the high-level cuts are discussed in the next section. For this purpose we have considered a sample size equivalent to 5 years of running in the HERON design. This would result, using the "standard" fiducial volume (see below), in 2.7×10^4 pp, 9.3×10^3 Be and 7.5×10^4 background events. However, in examining cut effects we studied six combinations of energy threshold cuts and fiducial cuts using the new PDF's appropriate to the cut combinations involved. The energy thresholds tested are at 30 and 45 keV, and the fiducial cuts paired with them are referred to as "small" ($-177.5\,\mathrm{cm} < z < 77.5\,\mathrm{cm}$, $R_{xy} < 230\,\mathrm{cm}$), "std" ($-187.5\,\mathrm{cm} < z < 87.5\,\mathrm{cm}$, $R_{xy} < 250\,\mathrm{cm}$), and "big" ($-208.5\,\mathrm{cm} < z < 108.5\,\mathrm{cm}$, $R_{xy} < 270\,\mathrm{cm}$), whose coordinate system is shown in Fig. 1. Interestingly, even though the S/N ratios can be very different depending on the cuts, the overall errors of fitted neutrino fluxes are much less sensitive.

5.4. *Errors in flux separation.*

Besides the statistical error on the total sample there are systematic errors in the flux separation process: error due to volume and threshold cuts as a result of spatial and energy resolution of the reconstruction, error from intrinsic uncertainty of the likelihood fitting method (arising as discussed in Sec. 5.1) and error due to uncertainty of absolute energy scale. We treat the latter error separately from the others.

Error due to volume and threshold cuts stems from the inaccuracy of spatial reconstruction of events. Given a set of N events, one can expect some N_a of them to be mistakenly accepted, while some other N_r of them to be mistakenly rejected. N_a and N_r can be modeled by comparing reconstructed events with their corresponding input values from our simulated event data, and the difference $N_a - N_r$ can be considered as a form of systematic bias of fitted flux, which could in principle be corrected for but the correction would be very small and of the same order as its error. Both N_a and N_r are subject to statistical fluctuations and such a correction will have an uncertainty $\sigma = \sqrt{N_a + N_r}$. This error depends on both spatial and energy cuts, and its values for some of their combinations are listed in Table. 2.

Errors of separated fluxes inherent to the likelihood method, as discussed in Sect. 5.1, are also calculated based on simulated neutrino and gamma event data. Since these errors depend on the shapes of the PDFs, which in turn depend on fiducial and energy cuts, they are listed in Table 3 in relation to the cuts also. The distributions of fitted energy are used to provide PDFs in the table.

It is worth noting that we are using only the PDF of one of the several fitted variables available. In principle, for example, we could fit the fluxes from both energy

	Volume	$E_{\rm thresh}$	Flux	N_a	N_r	σ/N
^{7}Be	big	30 keV	12899	345	256	0.19%
	std	45 keV	9345	236	169	0.22%
	small	45 keV	7339	184	127	0.24%
pp	big	30 keV	42123	2256	2037	0.16%
	std	45 keV	27000	1335	1233	0.19%
	small	45 keV	21163	1025	963	0.21%

Table 2
Flux error due to volume and threshold cuts, assuming event observed over a period 5 years. The definitions of N_a, N_r and volume sizes are given in text.

Volume	$E_{\rm thresh}$	$\varepsilon_{\rm Be}/N_{\rm Be}$	$\varepsilon_{\rm pp}/N_{\rm pp}$	ε_ν/N_ν
big	30 keV	2.48%	1.01%	1.00%
std	45 keV	2.48%	1.06%	1.08%
small	45 keV	2.56%	1.11%	1.10%

Table 3
Error inherent to the likelihood method using PDFs. εs are obtained from the error matrix V. ε_ν and N_ν are the error and total neutrino flux if the pp and ^{7}Be are not fitted separately. 5 years of observation is assumed.

and $\mathcal{L}(\mathbf{x})$ value PDFs, which, when combined, could lead to smaller fitting errors. However, there are significant correlations in fitted fluxes from energy and $\mathcal{L}(\mathbf{x})$, thus the combined fitting does not yield significant improvement over fitting using either variable separately. For simplicity, we currently choose to fit using only the energy PDFs, which have slightly smaller errors than those from the $\mathcal{L}(\mathbf{x})$.

Error induced by absolute energy scale uncertainty is a consequence of any energy threshold cut, because for events near the energy threshold, an error in energy scale may change its status of being accepted or rejected. This type of error is commonly described by the quantity $\frac{{\rm d}\Phi/\Phi}{{\rm d}E/E}$, which, when multiplied by the energy scale uncertainty $\delta E/E$, gives the relative error in flux Φ. Since the absolute energy scale uncertainty is a property of the physical detector system, it will be obtained by insertion of a calibration source. For purposes of this analysis it is assumed that a 2% uncertainty on the scale is achievable leading to a contribution to the pp flux error of 0.94% at a 45keV threshold. Based on our simulated fluxes, values for this quantity are listed in Table. 4. Note that this error depends on the energy threshold value but not the fiducial cut parameters, because the neutrino events are uniformly distributed throughout the detector volume. The calibration source would also be needed to establish the accuracy of the position reconstruction.

These three types of errors are all considered as systematic errors, and are independent of each other, thus will be summed in quadrature. Table 5 lists the combined error and the statistical fluctuations of the fitted fluxes (without the absolute energy scale uncertainty part, which should add another $\sim 1\%$ to pp and combined neutrino fluxes if we assume 2% absolute energy scale uncertainty). 5 years worth of observation at "std" fiducial cut and a 45 keV energy threshold are used in that table. For comparison, we also show in Table 5 the resulting errors to be expected when all optical effects are included. The differences are not significant as we have discussed in footnote 2.

	^{7}Be		pp	
$E_{\rm thresh}$	30	45	30	45
$\frac{{\rm d}\Phi/\Phi}{{\rm d}E/E}$	0.056	0.073	0.29	0.47

Table 4
Coefficient of error from absolute energy scale uncertainty.

	Statistical			Systematic			$\sigma_{\rm scale}$	
	^{7}Be	pp	^{7}Be+pp	^{7}Be	pp	^{7}Be+pp	^{7}Be	pp
non-opti	1.03%	0.61%	0.52%	2.49%	1.08%	1.10%	0.15%	0.94%
optical	1.03%	0.60%	0.52%	2.78%	1.21%	1.19%	$\sim 0.2\%$	$\sim 1\%$

Table 5
Relative statistical and systematic error of fitted neutrino fluxes. $\sigma_{\rm scale}$ column lists the error from absolute energy scale uncertainty of 2%. The terms "optical" and "non-optical" are defined in footnote 2.

6. Summary and Conclusions

We have described that, on the basis of the new knowledge gained in recent years of neutrino properties and of higher energy solar neutrino fluxes, there are excellent reasons to perform precision real-time measurements of the very low-energy neutrino fluxes from the Sun. The physics goals outlined in Sec. 2 include determining the luminosity of the Sun in neutrinos, providing checks on some details of the SSM, testing the MSW effect in the LMA solution and improving constraints on the neutrinos mass-mixing parameters as well as providing discovery opportunities in the new low energy regime.

To achieve these goals detectors are required which can measure the $\Phi_{\rm pp}$ flux with a precision better than 3% and the $\Phi_{\rm Be}$ flux to better than 5%. Such detectors must be capable of collecting very large event samples and maintain good control of systematic errors. We have described the design of such a possible detector, HERON, and have simulated its performance. Although the HERON detector is not presently scheduled or funded for construction, by experimentation in pro-

totypes of several liters we have measured the details of energy loss processes (scintillation, phonons/rotons, electron bubbles) for low energy electrons in the superfluid [34,35,38,40]. The development of wafer calorimeters capable of detecting all three channels has been carried out [41,42,43,44]. We have not tested an array of wafers as a coded aperture; however, given the well tested use of the method in other fields, performance as simulated can be reasonably expected. The superfluid helium target material is itself free of intrinsic internal background and provides two channels (scintillation and drifted electrons) to distinguish and separate externally entering background from point-like neutrino ES signals via an active coded-aperture array.

The simulation has been directed towards establishing the systematic and other errors to be expected for the HERON detector in an exposure of 5 years. For that purpose large samples of both signal and background events were generated and then fully reconstructed according to the physical processes in helium, the detector geometry and the properties of the coded aperture design. The expected signals were based on current best understanding of the neutrino mass-mixing parameters and the well-known electroweak scattering cross-sections. The backgrounds (gamma-ray conversions in the helium) were simulated from radioactive sources distributed throughout the major materials surrounding the helium. The level and nature of the activities assumed was in line with current best practice in solar and double beta decay neutrino experimentation. To separate a combined sample of pp, Be7 and backgrounds into their respective flux components, an extended loglikelihood method was used employing probability distribution functions constructed from various samples of the above simulation prescription. By design, the method included all correlations among variables imposed by event reconstruction, various cuts on the data as well as those arising from the properties of the PDF's themselves.

The results are quite promising as can be seen in Tables 2-5. It appears that should the detector be built and perform as modeled it would be capable of satisfying the criteria necessary for the precision pp and Be7 flux measurements. For example, to take the particular choice of the so-called "standard threshold and fiducial cut" on a 5-year exposure and combining all errors except energy scale (statistical, high-level cuts, likelihood method) a precision on pp flux of $\pm 1.35\%$ (or $\pm 1.68\%$ including energy scale uncertainty) results. Similarly for $\Phi_{\rm Be}$, we find errors of $\pm 2.96\%$ and $\pm 2.97\%$ without and with, respectively, the energy scale uncertainty included. The full neutrino flux obtained without attempting to employ the separation of $\Phi_{\rm pp}$ and $\Phi_{\rm Be}$ individually would present a combined error of $\pm 1.31\%$.

The validity of the background model used in these simulations is a key issue. The composition and relative magnitude of the background sources assumed were based on current experience in the field and should therefore be realizable in practice; nonetheless, it is important to ask to what extent are the simulation results dependent upon the assumed model and to what extent can the model be checked in practice. The decay modes of the sources, branching ratios and energies of the decay products are well known and the method of their propagation through the simulation programs are well established. Perhaps most important is the question of whether we may have mis-estimated the total background level and if so how strongly the result would be affected. A mistake in the magnitude would enter principally through the separation procedure using the PDF's; consequently we have tested this effect by varying the assumed size of the background over a wide range. The effect is not drastic; for example, should the background be 5 times larger, the $\Phi_{\rm pp}$ error would double while a factor 50 larger background would raise the $\Phi_{\rm pp}$ error by six times (however, this latter rate would introduce prohibitive wafer deadtime). In contrast, reducing the background by a factor of 0.5 only improves the $\Phi_{\rm pp}$ error by 15%.

In practice, there are some checks available on the model. Due to the good position and energy resolution for the point-like signal events, fiducial volumes of various sizes can be made and the stability of the flux results checked. As we have seen in Tables 2, 3 and 5, varying the high-level cuts by setting different fiducial volumes and thresholds does not have a strong effect upon the expected errors. Similarly, the nature and dependence of the observed spatial and energy distributions as a function of these cuts can also be compared directly to the model.

In conclusion we believe that a detector of the HERON design utilizing superfluid helium and a coded aperture array could provide the capability to carry out the multiple physics goals achievable through precision, real-time, simultaneous measurements of $\Phi_{\rm pp}$ and $\Phi_{\rm Be}$.

7. Acknowledgements

We are grateful to the U.S. Department of Energy for support of R&D on this project through grant DE-FG02-8840452. We are indebted to J.R. Klein for his close reading and valuable suggestions, R.B. Vogelaar for comments and A.W. Poon for assistance in providing

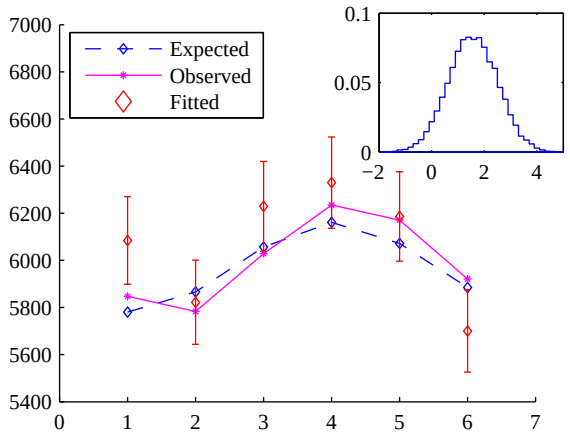

Fig. A.1. A typical fitting for Earth orbit eccentricity. (Inset: Normalized eccentricity results from 2×10^4 trial simulations.)

additional computing resources at Lawrence Berkeley National Laboratory.

Appendix A. Solar orbit eccentricity.

In order to examine the effectiveness of our flux fitting method under a more realistic context, we chose to test for the annual solar neutrino flux oscillation due to the Earth orbit eccentricity. The orbit of the Earth around the Sun has an eccentricity of $\sim 1.67\%$. Since the diameter of the Sun ($\sim 1.4 \times 10^6$ km) is much smaller than the radius of the orbit ($\sim 1.5 \times 10^8$ km), the Sun can be treated as a point source, thus the neutrino flux observed on Earth will oscillate according to $1/r^2$.

We simulated the number of events observed daily over a span of five years. These event numbers consist of both pp and ^{7}Be events including their statistical fluctuations. A random error according to the systematic uncertainty of the flux fitting method is then added to each day's flux, to simulate the errors introduced during the reconstruction and flux separation process. Then the daily fitted event counts are grouped into consecutive 60 day periods, with 5 days' worth of data each year discarded for simplicity. Thus over 5 years, each of these periods contain 300 days' worth of events. A χ^2 fit of these event numbers against the model of an elliptic Earth orbit can then be performed, using the eccentricity as the fitting parameter.

Figure A.1 shows a typical set of data for such fitting. The error bars on the "fitted" data include both statistical and systematic errors, as discussed in Sec. 5.4, where the absolute energy scale uncertainty is taken as 2%. Best fit of the particular data set in that figure gives an eccentricity of 2.1%; repeating this simulation for 2×10^4 times reveals the distribution of the best fitted eccentricity values to be $1.68\% \pm 0.95\% (1\sigma)$. This exercise demonstrates that our flux fitting method is capable of resolving the solar neutrino flux to the precision of a few percent given 5 years of detector running time.

References

[1] R.E. Lanou, H.J. Maris, G.M. Seidel, *Phys. Rev. Lett.* **58** (1987) 2498; S.R. Bandler, et al., *J. Low Temp Phys.* **93** (3/4) (1993) 715; R.E. Lanou, *Nucl. Phys. B. (Proc. Suppl.)* **138** (2005) 98.

[2] R.H. Dicke, *Astrophys. J.* **153** (1968) L101; J.G. Ables, *Proc. Astro. Soc. Aust.* **4** (1968) 172.

[3] K.E. Fenimore, T.M. Cannon, *Applied Optics* **17** (1978) 337.

[4] H.A. Bethe, *Phys. Rev. C* **55** (1939) 248; J.N. Bahcall, *"Neutrino Astrophysics"*, Cambridge University Press (1989)

[5] C. Arpesella et al, *arXiv:0708.2251v1 [astro-ph]*; G. Alimonti, et al., *Astroparticle Physics* **16** (2002) 205–234.

[6] D.N. McKinsey, J.M. Doyle (CLEAN; neon using ES), *J. Low Temp Phys.* **118** (2000) 153–165; Y. Suzuki (XMASS; xenon using ES), in: *Proc. LowNu2*, World Scientific Publ., 2001, p. 81; R. Raghavan (LENS; indium for ν_e flux), *Phys. Rev. Lett.* **78** (1997) 3618; H. Ejiri et al. (MOON; Mo for ν_e flux), *Phys. Rev. Lett.* **85** (14) (2000) 2917; C. Amsler et al. (CF4 TPC for ES) *arXiv:0710.1049v1 [hep-ex]*; M. Chen (SNO+; liquid scintilator for pep & CNO fluxes), *Earth, Moon and Planets* **99** (2006) 221.

[7] L. Wolfenstein, *Phys. Rev. D* **17** (1978) 2369; S.P. Mikheyev, A.Y. Smirnov, *Nuovo Cimento* **C9** (1986) 17.

[8] J.N. Bahcall, *Phys. Rev. C* **65** (2) (2002) 025801.

[9] C. Frohlich and J. Lean, *Geophys. Res. Lett.* **25** (1998) 4377.

[10] J.N. Bahcall, M.H. Pinsonneault and G.J. Wasserburg, *Rev. Mod. Phys.* **67** (4) (1995) 781–808.

[11] J.N. Bahcall, A.M. Serenelli and S. Basu, *Astrophys. J. Supplement Series* **165** (2006) 400.

[12] J.N. Bahcall, M. H. Pinsonneault and S. Basu, *Astrophys. J.* **555** (2001) 990.

[13] J.N. Bahcall, *Phys. Rev. Lett.* **12** (11) (1964) 300–302.

[14] J.N. Bahcall, *Phys. Rev. Lett.* **23** (5) (1969) 251–254.

[15] J.N. Bahcall, M. Fukugita and P. I. Krastev, *Phys. Lett. B* **374** (1996) 1–6.

[16] G. Fiorentini and B. Ricci, *Comments Mod. Phys. E* **1** (1999) 49–51.

[17] J.N. Bahcall and C. Peña-Garay, *J. High Energy Phys.* **11** (2003) 004.

[18] R.G.H. Robertson, *Prog. Part. Nucl. Phys.* **57** (2006) 90–105.

[19] A. Waple, *Prog. Phys. Geog.* **23** (1999) 309.

[20] D. Crommelynck, et al., *Geophys. Res. Lett.* **23** (1996) 2293.

[21] See e.g.: M. Spiro and D. Vignaud, *Phys. Lett. B* **242** (1990) 279; N. Hata, S. Bludman and P. Langacker, *Phys. Rev. D* **49** (1994) 3622; K. M. Heeger and R. G. H. Robertson, *Phys. Rev. Lett.* **77** (18) (1996) 3720–3723.

[22] G.L. Fogli, et al., *Phys. Rev. D* **66** (5) (2002) 053010.

[23] G.L. Fogli, et al., *Prog. Part. Nucl.* **57** (2006) 742.

[24] J.N. Bahcall and C. Peña-Garay, *New Journal of Physics* **6** (2004) 63; J.N. Bahcall, *Nucl. Phys. B (Proc. Suppl.)* **118** (2003) 77.

[25] J. N. Bahcall, M. C. Gonzalez-Garcia and C. Peña-Garay, *J. High Energy Phys.* **08** (2004) 016.
[26] M. Gonzalez-Garcia and M. Maltoni, *arXiv:0704.1800v1 [hep-ph]*; M. Maltoni, T. Schwetz, M.A. Tortola and J.W.F. Valle, *arXiv:hep-ph/0405172v6 Sept. 2007*.
[27] F. Confortola et al., *Phys. Rev. C* **75** (2007) 065803; *arXiv:0705.2151v1 [nucl-ex]* May (2007); T.A. Brown et al., *arXiv:0710.1279v3 [nucl-ex]* Oct. (2007).
[28] B.T. Cleveland, et al. (Homestake), *Astrophys. J.* **496** (1998) 505–526; W. Hampel, et al. (GALLEX), *Phys. Lett. B* **447** (1999) 127–133; J.N. Abdurashitov, et al. (SAGE), *Nucl. Phys. B* **118** (2003) 39; M. G. Altmann, et al. (GNO), *Phys. Lett. B* **616** (2005) 174; S.N. Ahmed, et al. (SNO), *Phys. Rev. Lett.* **92** (2004) 181301; Y. Fukuda, et al. (SuperK), *Phys. Lett. B* **539** (2002) 179; T. Araki, et al. (KamLAND), *Phys. Rev. Lett.* **94** (2005) 081801.
[29] J.N. Bahcall and M.H. Pinsonneault, *Phys. Rev. Lett.* **92** (12) (2004) 121301.
[30] See Ref. [26] p.66–102 for a general discussion and extensive references.
[31] A. Friedland, C. Lunardini and C. Peña-Garay, *Phys. Lett. B* **594** (2004) 347; O.G. Miranda, M.A. Tortola and J.W.F. Valle, *J. High Energy Phys.* **10** (2006) 008.
[32] R. Fardon, A.E. Nelson and N. Weiner, *J. Cosmol. Astropart. Phys* **0410** (2004) 005; M. Cirelli, M.C. Gonzalez-Garcia and C. Peña-Garay, *Nucl. Phys. B* **719** (2005) 219; V. Barger, P. Huber and D. Marfatia, *Phys. Rev. Lett.* **95** (2005) 211802; M.C. Gonzalez-Garcia, P.C. Holanda and R. Zukanovich Funchal, *Phys. Rev. D* **73** (2006) 033008.
[33] M. Maltoni, T. Schwetz, M.A. Tortola and J.W.F. Valle, *Phys. Rev. D* **68** (2003) 113010.
[34] J.S. Adams, *"Energy Deposition by Electrons in Superfluid Helium"*, Brown University PhD. Dissertation (2001).
[35] Y.H. Huang, *"Solar Neutrino Detection Utilizing a Variant of Coded Aperture on a Large Scale"*, Brown University PhD. Dissertation (2007).
[36] J.C. Hill, O. Heybey and G.K. Walters, *Phys. Rev. Lett.* **26** (1971) 1213; W. Stockton et al, *Phys. Rev. Lett.* **24** (1970) 654.
[37] H.J. Maris, *J. Low Temp. Phys.* **87** (1992) 773; S. Balibar, *Phys. Lett.* **51A** (1975) 455; S. Balibar et al, *Phys. Lett.* **60A** (1977) 135.
[38] S.R. Bandler et al, *Phys. Rev. Lett.* **74** (1995) 3169; S.R. Bandler, *"Detection of Charged Particles in Superfluid Helium"*, PhD. Dissertation, Brown University (1996); J.S. Adams et al, *Phys. Lett. B* **341(3/4)** (1995) 431.
[39] A.L. Fetter, in *"The Physics of Liquid and Solid Helium", Part I.* John Willey and Sons, (1976) Sec. 2.3.4.
[40] C.M. Surko and F. Reif, *Phys. Rev.* **175** (1968) 229; B. Sethumadhavan et al, *Nucl. Instr. Meth. A* **520** (2004) 142; B. Sethumadhavan, *"Charge Gain and Breakdown in Liquid Helium at Low Temperatures"*, PhD. Dissertation, Brown University (2007); B. Sethumadhavan et al, *Phys. Rev. Lett.* **97** (2006) 015301.
[41] A. Fleischmann et al, *Nucl. Instr. Meth. A* **520** (2004) 27; A. Fleischmann et al, *Nucl. Instr. Meth. A* **444** (2000) 100; S.R. Bandler et al, *J. Low Temp. Phys.* **93** (1993) 709.
[42] A. Fleischmann, C. Enss and G.M. Seidel, "Metallic Magnetic Calorimeters" in *Cryogenic Particle Detection*, Editor: C. Enss, Topics in Applied Physics Series, Springer Publ. (2005).
[43] B. Sethumadhavan et al, *Nucl. Instr. Meth. A* **520** (2004) 142.
[44] Y.H. Kim, *"Thermodynamics of Low Temperature Detectors"*, Brown University PhD. Dissertation (2004); Y.H. Kim et al, *Nucl. Instr. Meth. A* **520** (2004) 208.
[45] G.M. Seidel, R.E. Lanou and W. Yao, *Nucl. Instr. Meth. A* **489** (2002) 189.
[46] *Handbook of Optical Constants of Solids II*, Editor: E.D. Palik, Academic Press (1991).
[47] R. Brun et al, *Detector Description Program and Simulation Tool*, CERN, Geneva. (1993).
[48] L. Lyons, *Statistics for Nuclear and Particle Physicists*, Cambridge University Press (1986); G. Cowan, *Statistical Data Analysis*, Oxford University Press (1998).